PAPER

Fluorine-free dialkylphosphate-based ionic liquids as supercapacitor electrolytes

Sayantika Bhakta, Gaurav Tatrari, [ID] Andrei Filippov [ID] and Faiz Ullah Shah [ID] *

The synthesis and physicochemical and electrochemical properties of several fluorine-free ionic liquids (ILs) comprising dialkylphosphate anions coupled to N-heterocyclic cations such as pyrrolidinium (Pyrr), piperidinium (Pip), and pyridinium (Py) are presented. All the ILs are synthesized in a single step by reacting trialkyl phosphates with pyrrolidine, piperidine, or pyridine. These ILs exhibit ionic conductivities in the range of 0.07 to 0.57 mS cm^{-1} at 20 °C, while increasing to 3.98 mS cm^{-1} at 60 °C, and an electrochemical stability window (ESW) up to 6.8 V on a glassy carbon (GC) electrode. Furthermore, a comparative performance of symmetric supercapacitors (SCs) made of multiwalled carbon nanotubes (MWCNTs) using [EMPyrr][DEP] and [BMPyrr][DBP] as electrolytes is presented. The SC based on [EMPyrr][DEP] reveals higher capacity retention, a power density of 1050 W kg^{-1}, and an energy density of 68 Wh kg^{-1} using 0.5 A g^{-1} at 60 °C. This paves the way for developing fluorine-free and high-performant IL-based electrolytes for supercapacitors operating at elevated temperatures.

Introduction

The interest in supercapacitors (SCs) as sustainable energy storage devices is growing rapidly due to their high-power density, excellent cycling stability, and potential applicability in electric vehicles, portable electronic devices, and many different industrial equipment.[1,2] For efficient practical applications, their energy density needs to be improved while the self-discharge rate must be reduced.[3–6] To improve the performance of SCs, the development of efficient electrolytes is necessary. An electrolyte plays a crucial role in the overall performance of SCs, especially in improving their energy density, service life, and safety.[7,8]

Aqueous electrolytes have widely been used in SCs, but such electrolytes have a lower electrochemical window (ESW) up to 1.6 V and, therefore, produce low energy density. On the other hand, organic electrolytes are preferred over aqueous ones due to their wider ESWs. In this context, the most commonly studied commercial electrolyte for SCs is based on the tetraethylammonium tetrafluoroborate [TEA][BF$_4$] salt in acetonitrile that has a working voltage of about 2.7 V.[9,10] The [TEA][BF$_4$] salt has been extensively studied in the form of iongel and organic electrolytes.[11–14] The limitations of organic solvents, including acetonitrile, dimethyl carbonate, and propylene carbonate, are already well explored.[15–17] However, organic electrolytes also have major drawbacks, such as the flammability of the organic solvents, corrosion, and toxicity of the halogen moieties.

In stark contrast, ionic liquids (ILs) offer many beneficial properties of electrolytes, such as non-flammability, high thermal and electrochemical stabilities, and structural designability. However, more than 95% of all the studied ILs as SC electrolytes are based on fluorinated anions such as [BF$_4$] and [PF$_6$], which are unstable, cause corrosion and side reactions, and can be readily hydrolyzed.[18–20] Therefore, there is an urge to develop new and efficient electrolytes, which are fluorine-free and can meet the requirements of modern SCs in terms of thermal and electrochemical stabilities.

Among fluorine-free anions,[15–17] dialkylphosphate-based anions displayed beneficial properties, particularly in the context of safety concerns, as organophosphorus compounds have intrinsic flame-retardant properties.[21] These anions are pivotal in the optimization of separator and electrode materials, as well as in their utilization as electrolyte additives for overcharge protection and redox mediation.[22–24] Typically, ILs based on dialkylphosphate-based anions can be readily synthesized in a single step without any solvent using environmentally benign protocols.[25] Thus, ILs featuring phosphate-based fluorine-free anions are emerging as promising alternatives to the conventional fluorinated anions. Recently, we have reported two different types of fluorine-free structurally flexible phosphate-based ambient temperature liquid alkali metal salts and pyrrolidinium-, morpholinium- and imidazolium-based ILs as electrolytes with promising performance in batteries and supercapacitors.[26–29]

In this study, we report the synthesis, characterization, and electrochemical performance of fluorine-free ILs comprising diethylphosphate- and dibutylphosphate-based anions coupled to different cations (Fig. 1). The main aim is to investigate how

Chemistry of Interfaces, Luleå University of Technology, SE-971 87, Luleå, Sweden.
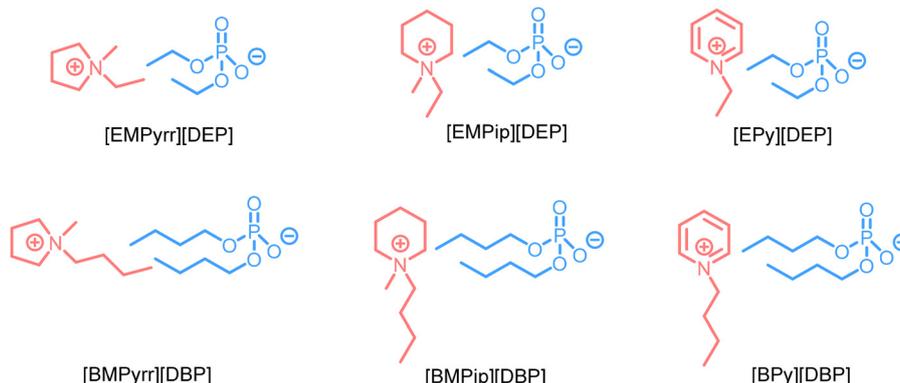*E-mail: faiz.ullah@ltu.se*

Fig. 1 Structures and abbreviations of the ionic components of the synthesized ILs.

the structure of these ILs influences the ion transport and electrochemical performance as a function of temperature. The ILs are investigated in terms of electrochemical stabilities, ionic conductivity and ion diffusion, specific capacitance, energy and power densities – all at variable temperatures.

2. Experimental

2.1. Materials, synthesis, and characterization

Triethyl phosphate (99% purity; Sigma Aldrich), tributyl phosphate (99% purity; Sigma Aldrich), 1-methylpyrrolidine (99% purity; Sigma Aldrich), pyridine (99%, Merck), N-methylpiperidine (99%, Acros organic), and ethyl acetate (Emsure, Merck) were used without any additional purification. The structures and purity of the synthesized ILs were confirmed using electrospray ionization mass spectrometry (ESI-MS) and multinuclear (^{1}H, ^{13}C, and ^{31}P) nuclear magnetic resonance (NMR) spectroscopy.

For ESI-MS, the samples were dissolved in acetonitrile and injected directly into Sciex Pulsar QTOF apparatus via a syringe pump at a rate of 150 microliters per minute. An external mass calibration was carried out while the device scanned from 50 to 800 Da at a rate of one scan per second. For NMR measurements, a Bruker Ascend Aeon WB 400 (Bruker BioSpin AG, Fällanden, Switzerland) spectrometer was used. For solution NMR experiments, the samples were dissolved in D$_2$O for all the experiments. The working frequencies were 400.21 MHz for ^{1}H, 100.64 MHz for ^{13}C, and 162.01 MHz for ^{31}P. Data were processed using Bruker Topspin 3.5 software. The ^{31}P NMR spectra of the neat ILs as a function of temperature were recorded by placing the sample in a 5 mm standard NMR tube. The detailed characterization and the ESI-MS (Fig. S1–S6) and the ^{1}H, ^{13}C, and ^{31}P NMR (Fig. S7–S24) spectra for each IL are presented in the supplementary information (SI). The freshly prepared ILs were kept in a vacuum oven at 80 °C for up to one week.

2.2. Electrode and cell preparation

The electrode material for supercapacitors was made of activated carbon from Nanografi (nano-powder size: <100 nm) combined with multiwalled carbon nanotubes (MWCNTs) from Sigma Aldrich (50–90 nm in diameter). Initially, MWCNTs, activated carbon, and PVDF were taken together and mixed in a ratio of 6:2:2 with N-methyl-2-pyrrolidone (NMP) to obtain a uniform slurry. MWCNTs

are highly conductive, whereas the activated carbon has a high surface area (400 m^2 g^{-1}). The 6:2:2 ratio (MWCNTs:activated carbon:PVDF) was selected to get benefits of all these components in terms of conductivity, porosity and binding properties.[30,31] This synergy is expected to enhance the ion transport and charge storage properties, especially in IL electrolytes where the ion sizes are larger than the conventional organic solvent-based electrolytes. The slurry was cast with a thickness of 160 mm on a thoroughly cleaned and dried battery-grade aluminum foil using a doctor's blade. Before being sliced into 14 mm electrodes, the prepared electrodes were dried in a vacuum oven at 80 °C overnight. The coin cell (CR 2032) supercapacitor devices were fabricated using two identical electrodes separated by an electrolyte-soaked separator (Whatman filter paper, GF/D grade).

2.3. Ionic conductivity

Electrochemical impedance spectroscopy (EIS) was used to assess ionic conductivity at frequencies ranging from 1 Hz to 1 MHz, with an AC voltage amplitude of 10 mV$_{rms}$. The measurements were carried out for both heating and cooling cycles within a temperature range of −20 to 100 ± 0.1 °C. A two-electrode system was used where a glassy carbon (GC) served as the working electrode (WE) and a 70 μL platinum (Pt) crucible as the sample container and counter electrode. Before each measurement, the electrodes were polished with 0.25 μm Kemet diamond paste. The cell constant was calculated using a Metrohm 100 μS cm^{-1} KCl standard solution (K_{cell} = 1.8736 cm^{-1}). The system was allowed to thermally equilibrate for 10 min before recording the impedance spectra.

The Vogel–Fulcher–Tammann (VFT) equation was used to simulate the temperature dependence of ionic conductivity (σ). The equation includes a pre-exponential factor σ_0, adjustable constants B and T_0, and the gas constant R. B is related to the glass transition temperature (T_g) and the system's activation energy (E_σ), where $E_\sigma = B \times R$. T_0 is the ideal vitreous transition temperature, which is the point at which configurational entropy equals zero.

$$\sigma = \sigma_0 \exp \frac{-B}{R(T - T_0)} \tag{1}$$

2.4. NMR diffusometry

Pulsed-field gradient (PFG) NMR diffusometry measurements were carried out on a Bruker Ascend Aeon WB 400 (Bruker

BioSpin AG) nuclear magnetic resonance (NMR) spectrometer with a working frequency of 400.21 MHz for ^{1}H and a Diff50 PFG NMR probe (Bruker). The greatest magnetic field gradient pulse amplitude was 29.73 T m^{-1}. Samples were placed inside the standard 5 mm NMR glass tube. Before each measurement, the sample was allowed to stabilize at a specified temperature for at least 20 minutes.

A molecule's diffusivity is measured by the diffusion decay (DD) of the amplitude (A) of the NMR spectral line, which is obtained by Fourier transforming the descending half of the stimulated echo (StE). This decay, as a function of the amplitude of the applied pulsed field gradient, can be represented by eqn (2) for a simple non-associating molecular liquid under the stimulated echo pulse sequence:

$$A(g,\delta,t_d) = A(0)\exp(-\gamma^2 g^2 \delta^2 D t_d) \tag{2}$$

Here, $A(0)$ represents the factor proportional to the proton content in the system, as well as the spin–lattice and spin–spin relaxation times. A is the integral intensity of the NMR signal, τ and τ_1 are the time intervals in the pulse train; g is the gyromagnetic ratio for magnetic nuclei; g and δ are the amplitude and the duration of the gradient pulse; $t_d = \left(\varDelta - \dfrac{\delta}{3}\right)$ is the diffusion time; $\varDelta = (\tau + \tau_1)$. D is the diffusion coefficient. In the measurements, δ was in the range of (0.5–3) ms, τ was in the range of (3–5) ms, and g varied from 0.06 up to 29.73 T m^{-1}. Diffusion time, t_d, varied from 20 to 100 ms. The recycle delay during the accumulation of signal transients was 5 s. Nonlinear least squares regression was used to fit the experimental data with eqn (3) to extract D values.

The diffusivity data are subjected to analysis by fitting into the following VFT eqn (3):

$$D = D_0 \exp\frac{-B}{R(T - T_0)} \tag{3}$$

The adjustable parameters, D_0, T_0, and B, are involved in determining the energy of activation for diffusion, where the activation energy (E_D) is correlated with B as $E_D = B \times R$. We characterized the temperature-dependent diffusion coefficient, $D(T)$, by fitting the parameters D_0, T_0, and B, and R is the gas constant.

2.5. Electrochemical measurements

To assess the electrochemical stability window (ESW) of the synthesized ILs, linear sweep voltammetry (LSV) was carried out using a three-electrode setup consisting of a GC as the working electrode (WE), a Pt cup as the counter electrode (CE), and an Ag wire coated with AgCl as the reference electrode (RE). The scan rate was 1 mV s^{-1} in all the experiments. The electrochemical potentials were recorded with ferrocene as the internal reference, and then the potential was adjusted to the Fc/Fc$^+$ couple standard. The ESW limits were determined using cut-off current densities of 0.1 and 0.5 mA cm^{-2}.

The coin cells were tested using a Biologic BCS-810 battery tester. To verify feasibility, stability, and reversibility, cyclic voltammetry (CV) was performed at 50 mV s^{-1} with a potential

window of 2 V. The CV was performed at 30 and 60 °C temperatures using variable scan rates ranging from 5 to 200 mV s^{-1}. Electrochemical impedance spectroscopy (EIS) was carried out at frequencies ranging from 0.01 to 10^6 Hz, and the galvanostatic charge–discharge (GCD) experiments were performed at various current densities. All the electrochemical studies were conducted in a closed cell placed within a temperature-controlled climate chamber. The specific capacitance (C_s) was calculated from CV and GCD using eqn (4) and (5), respectively.[32,33]

$$C_s = \frac{\int i\mathrm{d}V}{2mK\Delta V} \tag{4}$$

$$C_s = \frac{I\Delta t}{m\Delta V} \tag{5}$$

where C_s is the specific capacitance in F g^{-1}, $i\mathrm{d}V$ is the area under the CV curve, m is the mass in mg (1.5 mg each electrode), K is the scan rate in mV s^{-1}, ΔV is the potential window in V, I is the current in mA, and Δt is the discharge time. Finally, the energy density (E_D) and power density (P_D) were evaluated using eqn (6) and (7), respectively.[34,35]

$$\text{Energy density} = \frac{CV^2}{3.6 \times 2} \tag{6}$$

$$\text{Power density} = \frac{\text{Energy density} \times 3600}{\Delta t} \tag{7}$$

2.6. FTIR spectroscopy

A Bruker IFS 80v spectrometer was used to record accelerated total reflection (ATR-FTIR) spectra for Fourier transform infrared (FTIR) spectroscopy. The apparatus used a deuterated triglycine sulfate (DTGS) detector with a diamond ATR auxiliary to acquire data in double-sided forward-backward mode. The spectrum data were acquired for a total of 64 scans, co-added, and signal-averaged, at an optical resolution of 4 cm^{-1}.

3. Results and discussion

We begin with a discussion of the transport properties of the ILs, including ionic conductivity and ion diffusion as a function of temperature, along with the interactions between cations and anions analyzed using FTIR and NMR spectroscopy. Finally, application of the selected ILs as electrolytes in symmetric supercapacitors is demonstrated under different experimental conditions.

3.1. Transport properties

The ionic conductivity of these ILs with a common anion decreases in the order Py > Pyrr > Pip at lower temperatures, while, as expected, the ILs with a DEP anion display higher ionic conductivity than the ILs with a larger [DBP] anion (Table 1). Among these ILs, [EPy][DEP] exhibits the highest conductivity across at lower temperatures up to 25 °C (Fig. 2a).[36] This is primarily due to the positive inductive effect

Table 1 Molecular weights and ionic conductivities of the synthesized ILs

IL	MW	σ at 20 °C (mS cm^{-1})	σ at 60 °C (mS cm^{-1})
[EMPyrr][DEP]	267.31	0.39	3.98
[BMPyrr][DBP]	351.47	0.16	0.69
[EMPip][DEP]	281.33	0.223	2.10
[BMPip][DBP]	365.49	0.044	0.43
[EPy][DEP]	261.26	0.57	3.25
[BPy][DBP]	345.41	0.512	1.17

of the [EPy] cation from its alkyl chain, enhancing the electron density on the pyridinium ring and thus weakening the cation–anion interactions.[37] Unlike the aromatic ILs, the ionic conductivity of the non-aromatic [EMPyrr][DEP] ILs increases sharply with increasing temperature, indicating weaker ionic interactions with increasing temperature. Among these phosphate-based ILs, both the Pip-based ILs, [EMPip][DEP] and [BMPip][DBP], exhibit the lowest ionic conductivities throughout the studied temperature range, clearly reflecting the strongest cation–anion interactions in these systems. The VFT equation parameters support these observations, indicating a correlation between the ionic conductivity trends and the activation energy (E_σ) (Table S1). These phosphate-based ILs demonstrate slightly lower ionic conductivities compared to the conventional ILs based on fluorinated anions, but outperform the structurally analogous phosphate-based ILs containing long ether chains and also other fluorine-free reported ILs.[26–29,38,39]

To investigate the relative mobility of cations and anions in these ILs, PFG NMR diffusometry is employed. The self-diffusion coefficients of the cation (D_{cation}) and anion (D_{anion}) in all these ILs are about the same and cannot be distinguished by ^{1}H NMR spectroscopy (Fig. 2b). Therefore, D_{anion} was selectively determined using ^{31}P NMR spectroscopy (Fig. 2c), which confirmed comparable diffusivity as the D_{cation}. As expected, there is a continuous increase in the diffusivity of all ions with increasing temperature due to the dissociation of ions. For the same [DEP] anion, both the cation and anion in the [EMPyrr][DEP] IL exhibit faster diffusion compared to the ions in the [EPy][DEP] IL, suggesting that the ion–ion interactions play a

significant role. This is opposite to the ionic conductivity data, which is due to the aggregate formation in these systems. Since NMR diffusivity averages contributions from isolated ions, paired ions, and ion aggregates regardless of charges, the ionic conductivity data account for charged species. Thus, the opposite trend in diffusivity and ionic conductivity is associated with the aggregate formation in the [EPy][DEP] IL.

Similar to the [Pyrr]-based ILs, the ions in the [EMPip][DEP] IL diffuse more rapidly than their counterparts in the [BMPip][DBP] IL, due to the small size of cations and anions. Overall, [Pyrr]-based ILs demonstrate substantially higher ion mobility compared to [Py]- and [Pip]-based ILs throughout the measured temperature range. This trend is also obvious in the activation energy derived from the VFT equation (Tables S2 and S3). Activation energy increases with increasing size of the ions, and causes slower ion mobility, as also observed in ionic conductivity data.

3.2. Ionic interactions

The FTIR spectra exhibit all the characteristic bands associated with the synthesized ILs (Fig. 3). The [EMPyrr][DEP]-based ILs exhibit a P=O symmetric stretching band at 1238 cm^{-1}, whereas it is shifted to a lower wavenumber of 1231 cm^{-1} for [BMPyrr][DBP]. The same is true for the other ILs as well, implying a stronger ion–ion interaction for [DBP]-based ILs than the ILs based on the [DEP] anion (Fig. 3a). The strong peak at 1173 cm^{-1} in both [EPy][DEP] and [BPy][DBP] ILs is due to the C=C–N group in the cations, which is absent in all the other ILs (Fig. 3a).

The PO$_3$ stretching band at 1051 cm^{-1} in [EMPyrr][DEP] and [EMPip][DEP] ILs shifts to a higher wavenumber at 1066 cm^{-1} for [BMPyrr][DBP] and [BMPip][DBP] ILs (Fig. 3b). This band is slightly shifting towards a lower wavenumber for both [EPy][DEP] and [BPy][DBP] ILs. Furthermore, unlike [DEP]-based ILs, the [DBP]-based ILs display shoulders, implying different modes of interactions due to the delocalization of negative charge over oxygen to phosphorus.

The [DBP]-based ILs exhibit two stretching bands at 972 and 889 cm^{-1}, which are due to the O–P–O group of the [DBP] anion, which appears as a single band at 934 cm^{-1} for
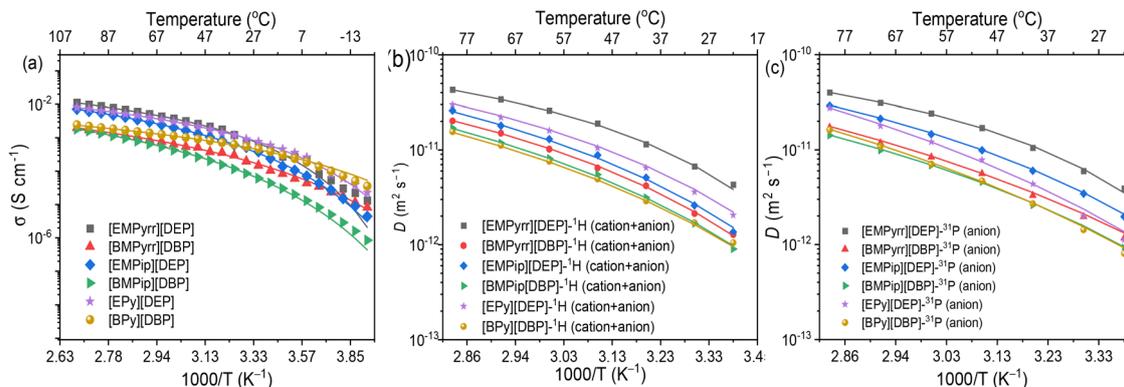

Fig. 2 (a) Ionic conductivities, (b) diffusion coefficients of cations and anions measured by ^{1}H NMR, and (c) diffusion coefficients of the phosphate anions measured by ^{31}P NMR of the ILs as a function of temperature. The symbols indicate the experimental data, and the solid lines represent the best fit to the VFT equation.
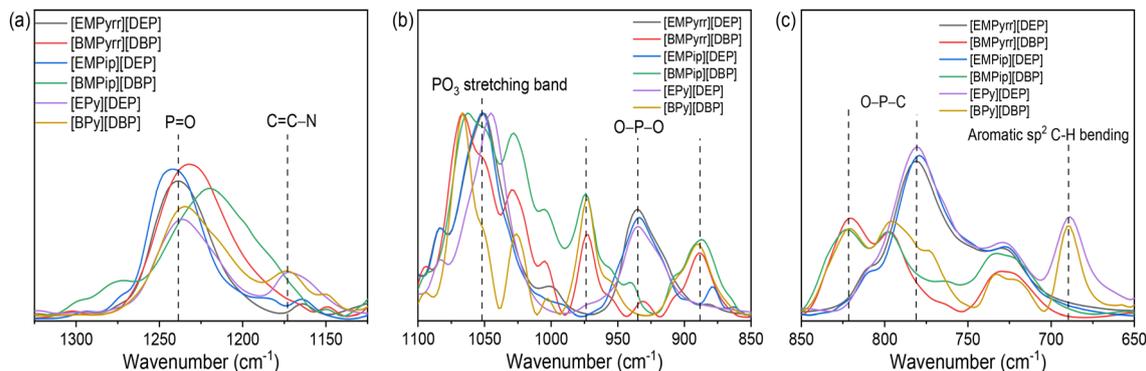
Fig. 3 FTIR spectra (a)–(c) of the the synthesized ILs.

[DEP]-based ILs. Again, the two bands associated with the O–P–O group for the [DBP]-based ILs are attributed to different modes of interaction in these ILs. The [DBP]-based ILs display two stretching bands at 820 and 795 cm^{-1} for O–P–C of the anion, while this appears as a single band at 780 cm^{-1} in the [DEP]-based ILs. Different from other ILs, the presence of a strong peak at 688 cm^{-1} is associated with the aromatic protons in the [Py]-based ring of the cation (Fig. 3c).

Since the anion plays a critical role in the ionic interactions of these phosphate-based ILs, ^{31}P NMR spectroscopy is employed to gain insights into the local environment of the phosphorous atom of the anions (Fig. 4 and 5). Although all the phosphate ILs reveal a single ^{31}P resonance line, the chemical shift is significantly influenced by the counter cation,[40] reflecting differences in the electronic environment surrounding the phosphate group (Fig. 4). In addition to the changes in chemical shifts, ^{31}P resonance lines display different shapes and broadness. For example, the ^{31}P resonance line for [BMPip][DBP] is much broader than all the others, which is due to the slower dynamics and reorientation dynamics of the [DBP] anion in this IL.[40] The [EMPyrr][DEP] and [EMPip][DEP] ILs exhibit upfield ^{31}P resonance lines approaching −1 ppm.
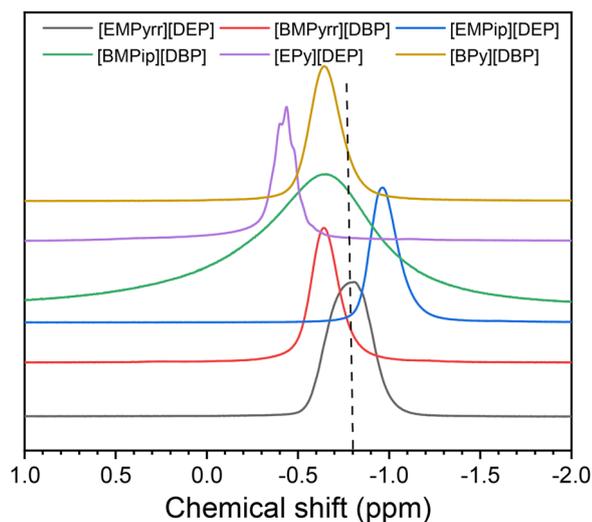
Conversely, the ^{31}P resonance line for the [EPy][DEP] IL containing the same anion is shifted downfield, *ca.* −0.4 ppm. This might be due to the weaker ionic interactions caused by the symmetric [EPy] cations, which is also reflected by the higher ionic conductivity of the [EPy][DEP] IL. In comparison, the [BMPyr][DBP] and [BMPip][DBP] ILs demonstrate relatively downfield resonance ^{31}P lines at −0.65 ppm, suggesting a less electrochemically shielded phosphorus environment caused by weaker ionic interactions.

The change in chemical shifts and broadness of the ^{31}P NMR spectra with increasing temperature reveals changes in the strength of ion–ion interactions (Fig. 5a–f). The ^{31}P resonance line of [EMPyrr][DEP] remains almost unchanged with increasing temperature (Fig. 5a), whereas the ^{31}P resonance line for the structurally analogous [BMPyrr][DBP] IL shifts to a higher ppm, indicating structural changes in the bulkier [DBP] anion as a result of ion dissociation (Fig. 5b). This may also be due to the thermal expansion of the sample, leading to a weakening of the interionic interaction. Fig. 5e shows splitting in the spectrum, which decreases as the temperature increases. NMR spectrum splitting disappears with increasing temperature due to dynamic averaging effects that occur when molecular motion or proton exchange rates exceed the NMR detection timescale.[41]

In contrast, the [EMPip][DEP] IL shows relatively smaller shifts with increasing temperature (Fig. 5c). The [BMPip][DBP] IL exhibits a much broader ^{31}P resonance line at ambient temperature, although the broadness is significantly reduced with increasing temperature (Fig. 5d). Among these phosphate-based ILs, [EPy][DEP] and [EPy][DEP] ILs demonstrate the most downfield shift with increasing temperature, where the interactions are dominated by the π–π stacking in pyridinium cations (Fig. 5e and f). Moreover, the shorter ethyl chains in [EPy][DEP] reduce steric hindrance, leading to a less electronically shielded phosphorus environment with increasing temperature. The line broadness clearly indicates slower ion mobility, which agrees well with ionic conductivity and ion diffusion data.

3.3. Electrochemical assessments

The ESWs of ILs are greatly influenced by the selection of the cut-off current density of the cathodic and anodic limits.
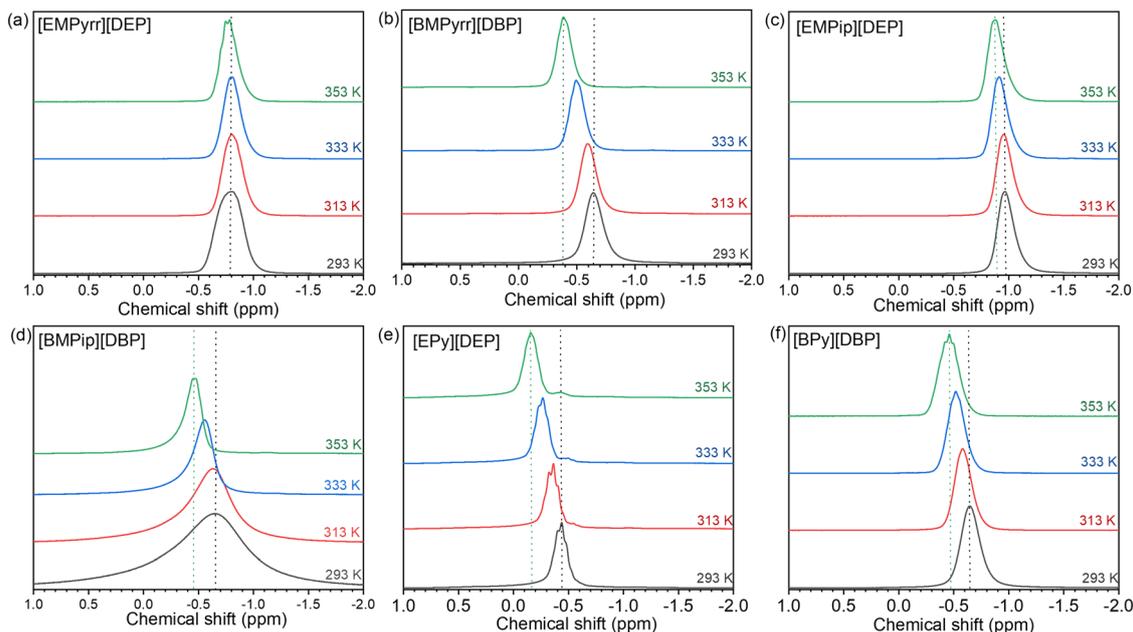

Fig. 4 ^{31}P NMR spectra of the neat ILs at ambient temperature.

Fig. 5 ^{31}P NMR spectra of the neat ILs (a)–(f) as a function of temperature.

The commonly used cut-off current densities are 0.01, 0.5, 1, and 5 mA cm^{-2} for realistic representation of the ESWs of ILs.[35] Here, we preferred to use 0.1 and 0.5 mA cm^{-2} as the cut-off current densities to provide a better picture of the electrochemical behavior of these ILs. The synthesized ILs display ESWs in the range from 1.6 to 3.6 V at a cut-off current density of 0.1 mA cm^{-1}, while the windows are significantly wider up to 6.7 V at 0.5 mA cm^{-1} (Fig. 6 and Table S4). For the same anion, either DEP or DBP, the ESW of the IL decreases as Pip > Pyrr > Py, which agrees well with the ESWs of other ILs calculated by computational data.[35] Among these ILs, Py-based ILs display lower electrochemical stabilities compared to ILs based on Pyrr- and Pip-cations due to the presence of double bonds.[42] In addition, the ILs with a larger DBP anion exhibit wider ESWs than the smaller DEP anions.
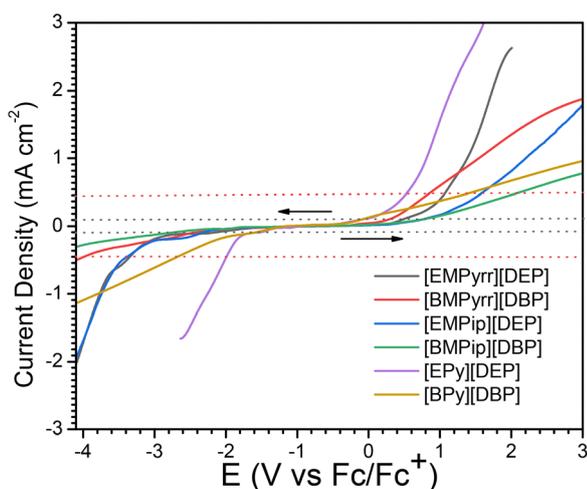

Fig. 6 LSV curves with cathodic and anodic scans of the ILs at ambient temperature using GC as the WE.

Based on the ionic conductivity and electrochemical stability data, [EMPyrr][DEP] and [BMPyrr][DBP] ILs are selected as electrolytes for SCs. The variable voltage CV curves performed at 30 °C suggest that both electrolytes exhibit promising electrochemical stabilities in symmetric SC devices (Fig. 7). Furthermore, the variable-voltage CV data at 100 mV s^{-1} are used to examine both the cathodic and anodic limits. The [EMPyrr][DEP]-based SCs exhibit greater current over a wider potential window compared to [BMPyrr][DBP]-based SCs (Fig. S25 and S26).

Comparing the capacitive performance of [EMPyrr][DEP] and [BMPyrr][DBP] electrolytes, the former shows a much better performance at both 30 °C and 60 °C (Fig. 8a–d), which is attributed to its smaller cation and anion, higher ionic conductivity, and faster ion diffusivity.[28,29] As expected, the specific capacitance increases with increasing temperature and decreases with increasing scan rate (Fig. S27a–d), facilitated by the higher ionic mobilities and improved thermal stability.[39] The maximum specific capacitances of 162 and 149 F g^{-1} are observed for SCs with [EMPyrr][DEP] and [BMPyrr][DBP] electrolytes at 5 mV s^{-1} and 30 °C, respectively. While increasing the temperature from 30 to 60 °C, the performance is significantly improved to 216 and 173 F g^{-1} at the same scan rate of 5 mV s^{-1} for SCs with [EMPyrr][DEP] and [BMPyrr][DBP] electrolytes, respectively (Table S5).

The enhanced performance at elevated temperature is likely due to the improved ion mobility, better electrolyte–electrode interfacial contact, and reduced resistance, leading to efficient charge transfer and ion diffusion, thereby promoting stable and reversible electrochemical behavior. In this context, the [EMPyrr][DEP] IL-based SC exhibits conventional capacitive behavior and a uniform current–potential vacillation, whereas the [BMPyrr][DBP] IL-based SC exhibits poor capacitive performance.
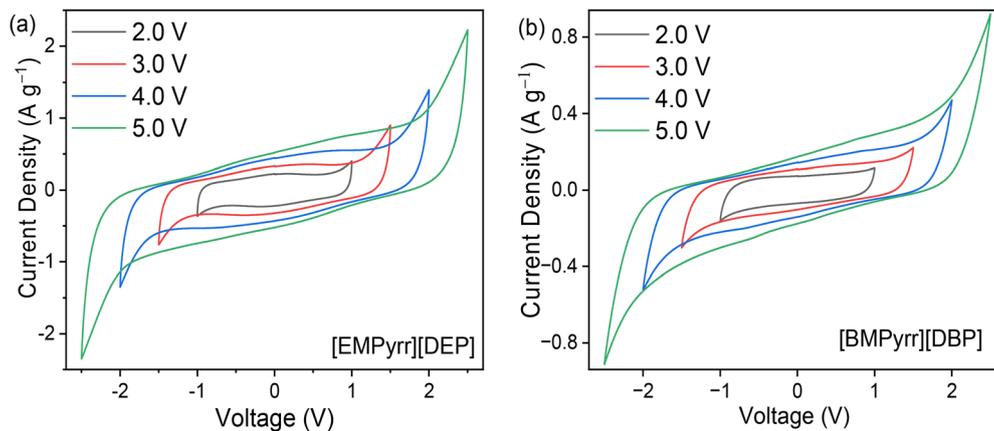
Fig. 7 CV curves of the SCs at 50 mV s^{-1} using (a) [EMPyrr][DEP] and (b) [BMPyrr][DBP] electrolytes at 30 °C.

As the scan rate increased from 5 to 200 mV s^{-1}, the specific capacitance is retained by 30% at 60 °C and 29% at 30 °C for the SCs with [EMPyrr][DEP] electrolyte. This indicates a minimal loss of capacitance due to the reduced retention time of the electrolyte ions.[43] However, a slightly higher loss of capacitance with increasing scan rate is observed for the SCs with [BMPyrr][DBP] electrolyte, which is associated with the bulky ions of this IL.[44]

The better energy storage capabilities of the [EMPyrr][DEP] electrolyte compared to [BMPyrr][DBP] are attributed to the increased ion mobility and reduced resistance as evidenced from the EIS data (Fig. S28).[45,46] The Nyquist plots of both SCs

displayed a decrease in sheet resistance (R_s) and charge transfer resistance (R_{ct}) with increasing temperature (Table S6). The R_s value of the SC with [EMPyrr][DEP] electrolyte reduced significantly from 24 Ω at 30 °C to 9 Ω at 60 °C, while R_{ct} diminished from 272 Ω at 30 °C to 126 Ω at 60 °C. In contrast, the R_s of the device with the [BMPyrr][DBP] electrolyte decreased from 260 to 73 Ω on increasing the temperature from 30 to 60 °C, while R_{ct} decreased from 720 to 314 Ω. This decrease in R_s indicates reduced internal resistance at a higher temperature as a result of improved ion mobility within the device.[47–49]

Additionally, the elevated temperature double-layer behavior of the SCs is confirmed by the charge–discharge data at 60 °C,
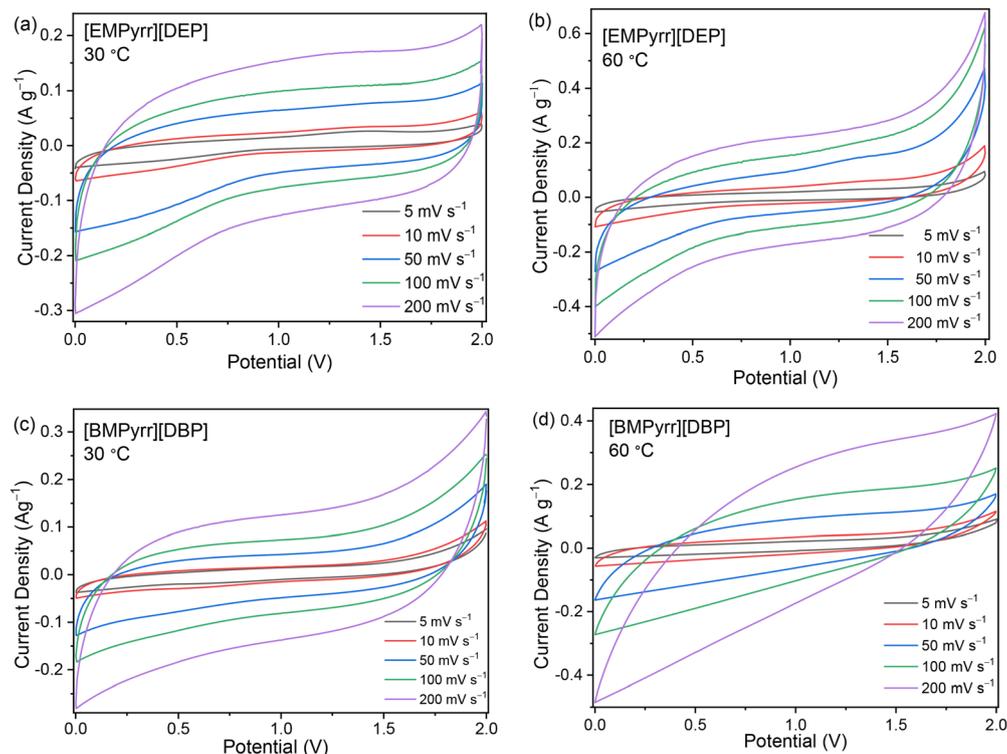

Fig. 8 CV curves of the SCs with (a) and (b) [EMPyrr][DEP], and (c) and (d) [BMPyrr][DBP] electrolytes at 30 °C and 60 °C.
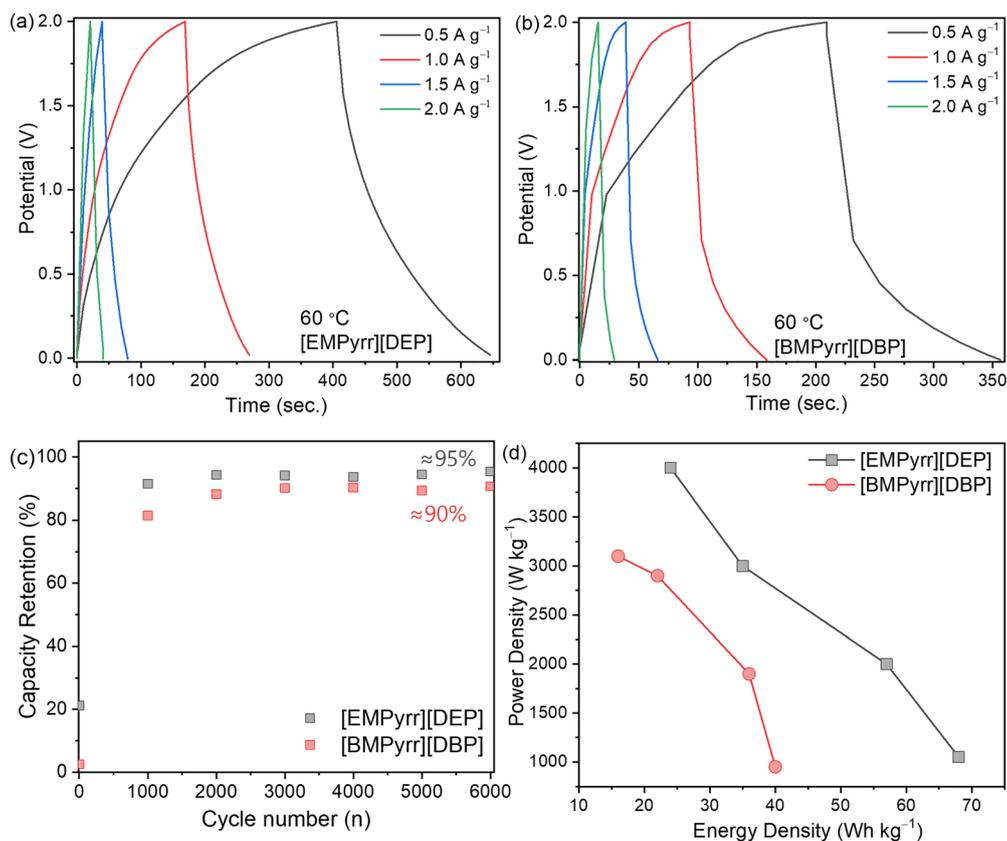
Fig. 9 GCD curves of the SCs with (a) [EMPyrr][DEP] and (b) [BMPyrr][DBP] electrolytes at 60 °C. (c) Capacity retention and (d) Ragone plots of the SCs using [EMPyrr][DEP] and [BMPyrr][DBP] electrolytes.

which exhibit a triangular shape for both the devices (Fig. 9a, b and Table S7). Once again, the [EMPyrr][DEP]-based SC outperformed the [BMPyrr][DBP]-based SC, displaying specific capacitances of 120 and 103 F g^{-1} at current densities of 0.5 A g^{-1} and 1 A g^{-1}, respectively, compared to 75 and 66 F g^{-1} for the device with [BMPyrr][DBP] electrolyte.

As expected, the specific capacitance decreased with increasing current density, demonstrating the typical double-layer behavior.[50,51] At lower current densities, there is more time for the electrolyte ions to migrate and accumulate at the electrode–electrolyte interfaces, leading to the formation of a thicker double layer and resulting in a higher capacitance.[51,52] Furthermore, the device with [EMPyrr][DEP] electrolyte benefits from the faster ion mobility, with a minimal resistance at the electrolyte–electrode interfaces, *i.e.*, polarization effect during charge–discharge cycles.[53] The thermal and electrochemical stabilities of these electrolytes provide longevity and consistent performance over extended cycles by preventing electrolyte drying and degradation.[48]

The elevated temperature (at 60 °C) long-term cyclic stability data display a capacity retention of 95% over 6000 cycles at 2 A g^{-1} for the SC with [EMPyrr][DEP] electrolyte and 90% for the SC with [BMPyrr][DBP] electrolyte (Fig. 9c and Fig. S29). The charge–discharge curves exhibit slight distortion during the initial cycles, likely due to the initial internal resistance, but

then improved in the subsequent cycles.[49] The SC with [EMPyrr][DEP] electrolyte allows for a higher proportion of electrons to be transferred during the charge and discharge processes compared to the SC with [BMPyrr][DBP].[54] As a consequence, the SC with [EMPyrr][DEP] electrolyte has a slight loss in capacitance during each charge–discharge cycle, which implies a longer potential lifespan.[55] In terms of power and energy densities, the SC with [EMPyrr][DEP] electrolyte outperforms the device with [BMPyrr][DBP] electrolyte (an energy density of 68 Wh kg^{-1} *vs.* 42 Wh kg^{-1} at 0.5 A g^{-1}, and a power density of 1050 W kg^{-1} *vs.* 950 W kg^{-1} at 0.5 A g^{-1}). In addition, for the SC with [EMPyrr][DEP] electrolyte, the power density increases from 1050 W kg^{-1} to 4000 W kg^{-1} with increasing current density from 0.5 A g^{-1} to 2.0 A g^{-1} (Fig. 9d and Table S8). The energy and power densities of our electrolytes are higher and/or comparable with those of the recently reported fluorine-free and fluorinated IL-based electrolytes (Fig. S30 and Table S9).[28,56–58]

4. Conclusions

Six new fluorine-free dialkylphosphate-based ILs synthesized using a solvent-free direct alkylation method revealed promising ion transport and electrochemical properties. A systematic structure–property relationship was established, where the

pyrrolidinium-based ILs exhibited better physicochemical and electrochemical properties, while the pyridinum-based ILs offered better ionic conductivities, and piperidinium-based ILs exhibited wider ESWs. In terms of electrolyte performance, the symmetric supercapacitor based on the [EMPyrr][DEP] IL outperformed the supercapacitor with the [BMPyrr][DBP] IL as an electrolyte primarily due to the small ion sizes and higher ionic conductivity of the former IL. These results highlight that introducing phosphate groups into ILs not only addresses the flammability and safety issues of electrolytes but also significantly enhances the electrochemical performance of supercapacitors. Overall, this study is a step towards functional fluorine-free ILs and electrolytes for energy storage applications.

Conflicts of interest

There are no conflicts to declare.

Data availability

The data supporting this article have been included as part of the supplementary information (SI). Supplementary information is available. See DOI: https://doi.org/10.1039/d5ya00217f.

Acknowledgements

References

1 M. S. Asl, R. Hadi, L. Salehghadimi, A. G. Tabrizi, S. Farhoudian, A. Babapoor and M. Pahlevani, *J. Energy Storage*, 2022, **50**, 104223.

2 J. Yang, M. Li, S. Fang, Y. Wang, H. He, C. Wang, Z. Zhang, B. Yuan, L. Jiang, R. H. Baughman and Q. Cheng, *Science*, 2024, **383**, 771.

3 Q. Zhang, J. Rong, D. Ma and B. Wei, *Energy Environ. Sci.*, 2011, **4**, 2152.

4 R. Yi, S. Chen, J. Song, M. L. Gordin, A. Manivannan and D. Wang, *Adv. Funct. Mater.*, 2014, **24**, 7433.

5 J. Yan, Q. Wang, T. Wei and Z. Fan, *Adv. Energy Mater.*, 2014, **4**, 1300816.

6 K. Liu, C. Yu, W. Guo, L. Ni, J. Yu, Y. Xie, Z. Wang, Y. Ren and J. Qiu, *J. Energy Chem.*, 2021, **58**, 94.

7 J. Ding, Y. Yang, J. Poisson, Y. He, H. Zhang, Y. Zhang, Y. Bao, S. Chen, Y. M. Chen and K. Zhang, *ACS Energy Lett.*, 2024, **9**, 1803.

8 Y. S. Meng, V. Srinivasan and K. Xu, *Science*, 2022, **378**, eabq3750.

9 F. Cheng, X. Yu, J. Wang, Z. Shi and C. Wu, *Electrochim. Acta*, 2016, **200**, 106.

10 E. Perricone, M. Chamas, J.-C. Leprêtre, P. Judeinstein, P. Azais, E. Raymundo-Pinero, F. Béguin and F. Alloin, *J. Power Sources*, 2013, **239**, 217.

11 M. Deschamps, E. Gilbert, P. Azais, E. Raymundo-Piñero, M. R. Ammar, P. Simon, D. Massiot and F. Béguin, *Nat. Mater.*, 2013, **12**, 351.

12 C. Yang, M. Sun, X. Wang and G. Wang, *ACS Sustainable Chem. Eng.*, 2015, **3**, 2067.

13 C.-H. Yang, Q. D. Nguyen, T.-H. Chen, A. S. Helal, J. Li and J.-K. Chang, *ACS Sustainable Chem. Eng.*, 2018, **6**, 1208.

14 A. Kumar, B. N. Mahanty, A. Rawat, R. Muhammad, R. K. Panigrahi, D. Pradhan and P. Mohanty, *Energy Fuels*, 2023, **37**, 6810.

15 M. Salari, J. C. Varela, H. Zhang and M. W. Grinstaff, *Mater. Adv.*, 2021, **2**, 6049.

16 D. Luo, M. Li, Y. Zheng, Q. Ma, R. Gao, Z. Zhang, H. Dou, G. Wen, L. Shui and A. Yu, *Adv. Sci.*, 2021, **8**, 2101051.

17 S. T. Gunday, E. Cevik, S. Asiri, A. Iqbal, A. Almofleh, A. N. Alqarni, I. Anil, O. Alagha and A. Bozkurt, *Energy Fuels*, 2022, **36**, 13229.

18 M. G. Freire, C. M. S. S. Neves, I. M. Marrucho, J. A. P. Coutinho and A. M. Fernandes, *J. Phys. Chem. A*, 2010, **114**, 3744.

19 S. Beil, M. Markiewicz, C. S. Pereira, P. Stepnowski, J. Thöming and S. Stolte, *Chem. Rev.*, 2021, **121**, 13132.

20 C. Yue, P. Sun and F. Li, in *Encyclopedia of Ionic Liquids*, ed. S. Zhang, Springer Nature Singapore, Singapore, 2022, pp. 1004–1026.

21 A. Marklund, B. Andersson and P. Haglund, *J. Environ. Monit.*, 2005, **7**, 814.

22 J. Wang, Y. Yamada, K. Sodeyama, E. Watanabe, K. Takada, Y. Tateyama and A. Yamada, *Nat. Energy*, 2018, **3**, 22.

23 Z. Zeng, V. Murugesan, K. S. Han, X. Jiang, Y. Cao, L. Xiao, X. Ai, H. Yang, J. G. Zhang, M. L. Sushko and J. Liu, *Nat. Energy*, 2018, **3**, 674.

24 H. Cavers, P. Molaiyan, M. Abdollahifar, U. Lassi and A. Kwade, *Adv. Energy Mater.*, 2022, **12**, 2200147.

25 E. Kuhlmann, S. Himmler, H. Giebelhaus and P. Wasserscheid, *Green Chem.*, 2007, **9**, 233.

26 S. Bhowmick, M. Ahmed, A. Filippov, L. C. Loaiza, F. U. Shah and P. Johansson, *Chem. Commun.*, 2023, **59**, 2620.

27 S. Bhowmick, A. Filippov, I. A. Khan and F. U. Shah, *Phys. Chem. Chem. Phys.*, 2022, **24**, 23289.

28 S. Bhowmick, G. Tatrari, A. Filippov, P. Johansson and F. U. Shah, *Phys. Chem. Chem. Phys.*, 2023, **25**, 19815.

29 G. Tatrari, S. Bhowmick, A. Filippov, R. An and F. U. Shah, *Energy Storage*, 2024, **6**(1), e535.

30 M. M. Baig, M. A. Khan, I. H. Gul, S. U. Rehman, M. Shahid, S. Javaid and S. M. Baig, *J. Electron. Mater.*, 2023, **52**, 5775.

31 G. Xu, C. Zheng, Q. Zhang, J. Huang, M. Zhao, J. Nie, X. Wang and F. Wei, *Nano Res.*, 2011, **4**, 870.

32 G. Tatrari, M. Karakoti, C. Tewari, S. Pandey, B. S. Bohra, A. Dandapat and N. G. Sahoo, *Mater. Adv.*, 2021, **2**, 1454.

33 M. Pathak, D. Bhatt, R. C. Bhatt, B. S. Bohra, G. Tatrari, S. Rana, M. C. Arya and N. G. Sahoo, *Chem. Rec.*, 2024, 24.

34 G. Tatrari, M. Ahmed and F. U. Shah, *Coord. Chem. Rev.*, 2024, **498**, 215470.

35 Z. Xue, L. Qin, J. Jiang, T. Mu and G. Gao, *Phys. Chem. Chem. Phys.*, 2018, **20**, 8382.

36 B. K. Mishra and N. Sathyamurthy, *J. Phys. Chem. A*, 2005, **109**, 6.

37 S. Men, P. Licence, H. Luo and S. Dai, *J. Phys. Chem. B*, 2020, **124**, 6657.

38 I. A. Khan, O. I. Gnezdilov, Y.-L. Wang, A. Filippov and F. U. Shah, *J. Phys. Chem. B*, 2020, **124**, 11962.

39 M. Ahmed, G. Tatrari, P. Johansson and F. U. Shah, *ACS Sustainable Chem. Eng.*, 2024, **12**, 16896.

40 R. Nanda and K. Damodaran, *Magn. Reson. Chem.*, 2018, **56**, 62.

41 M. H. Levitt, *Spin dynamics: basics of nuclear magnetic resonance*, John Wiley & Sons, 2008.

42 B. Dilasari, Y. Jung, G. Kim and K. Kwon, *ACS Sustainable Chem. Eng.*, 2016, **4**, 491.

43 N. Chen, Y. Pang, Z. Liu, N.-L. Shen, H. Chen, W. Zhang, Q. Lai, X. Yi and Y. Liang, *ACS Nano*, 2024, **18**, 32205.

44 Y. Huang, L. Ning, X. Zhang, Q. Zhou, Q. Gong and Q. Zhang, *Chem. Soc. Rev.*, 2024, **53**, 1090.

45 V. S. Cvetković, V. D. Jović, N. D. Nikolić, T. S. Barudžija, S. Dimitrijević and J. N. Jovićević, *J. Electroanal. Chem.*, 2024, **958**, 118161.

46 E. J. Park, P. Jannasch, K. Miyatake, C. Bae, K. Noonan, C. Fujimoto, S. Holdcroft, J. R. Varcoe, D. Henkensmeier and M. D. Guiver, *Chem. Soc. Rev.*, 2024, **53**, 5704.

47 A. C. Lazanas and M. I. Prodromidis, *ACS Meas. Sci. Au*, 2023, **3**, 162.

48 Y. Yang, M. Liu, D. Zhang, S. Wu and W. Zhang, *Battery Energy*, 2025, e20240089.

49 K. Zhang, C. Wang, X. Luo, Y. Pan, G. Li and K. Wang, *ACS Sustainable Chem. Eng.*, 2024, **12**, 6059.

50 Q. Dou, N. Wu, H. Yuan, K. H. Shin, Y. Tang, D. Mitlin and H. S. Park, *Chem. Soc. Rev.*, 2021, **50**, 6734.

51 S. Xu, H. Qiu, S. Jiang, J. Jiang, W. Wang, X. Xu, W. Kong, T. D. Chivurugwi, A. Proskurin and D. Chen, *Nano Res.*, 2024, **17**, 8086.

52 M. A. Qamar, M. Y. Almashnowi, M. H. J. Mashniwi, S. K. Ali and N. Shahadat, *Ionics*, 2025, **31**(4), 3121.

53 N. Choudhary, A. Tomar, S. Singh, R. Chandra and P. K. Maji, *Nanoscale*, 2025, **17**, 1289.

54 Z. Zhang, H. Wang, K. Yang, F. Zhang, Y. Li, B. Xue and X. Gu, *Appl. Clay Sci.*, 2025, **265**, 107661.

55 R. Yuan, H. Jiao, X. Du, L. Li, Q. Liu and S. Jiao, *ACS Nano*, 2025, **19**(4), 4694.

56 S. Bhakta, G. Tatrari, M. Rudakova, A. Filippov and F. U. Shah, *Chem. Eur. J.*, 2025, e01641.

57 P. F. R. Ortega, G. A. D. Santos, J. P. C. Trigueiro, G. G. Silva, N. Quintanal, C. Blanco, R. L. Lavall and R. Santamaría, *J. Phys. Chem. C*, 2020, **124**, 15818.

58 Z. Bo, X. Zhang, Z. Huang, Y. Huang, J. Yan, K. Cen and H. Yang, *RSC Adv.*, 2023, **13**, 15762.